Journal of Geophysical Research: Earth Surface

Supporting Information for

Inferring the Subsurface Geometry and Strength of Slow-moving Landslides using 3D Velocity Measurements from the NASA/JPL UAVSAR

A. L. Handwerger[1,2], A. M. Booth[3], M. -H. Huang[4], and E. J. Fielding[2]

[1]Joint Institute for Regional Earth System Science and Engineering, University of California, Los Angeles, CA, USA
[2]Jet Propulsion Laboratory, California Institute of Technology, Pasadena, CA, USA
[3]Department of Geology, Portland State University, Portland, OR, USA
[4]Department of Geology, University of Maryland, College Park, MD, USA

Contents of this file

Text S1 to S2
Figures S1 to S9
Tables S2 and S4

Additional Supporting Information (Files uploaded separately)

Captions for Tables S1 and S3

Text S1.

Inclinometer measurements at Two Towers landslide, northern California Coast Ranges

The Two Towers landslide, located in our field area in the northern California Coast Ranges (Figure 1), is a USGS long term monitoring station that has three inclinometers installed at "upper", "middle", and "lower" sites (Schulz et al., 2018). The inclinometers are arrays of 16 sensors with a minimum resolution of ~0.3 m installed in PVC placed in the borehole. Nearly all deformation at the "upper" borehole occurs between 6.2-6.5 m below the ground surface. The deformation at the "lower" borehole occurs between 3.3 to 3.9 m below the ground surface. Unfortunately, the sliding surface is located below the bottom of the "middle" borehole.

Using the borehole data from the Two Towers landslide (Figure S1), we constrain f following the formulation derived by Delbridge et al., (2016)

$$f_n = \frac{(2n+1)-nY/h}{2n+1}, \qquad \text{(S1)}$$

where Y is the height of the yield surface, H is the total depth, and n is the flow index equal to 1 and 3. We calculate four values of f from the two boreholes $f_{1,\text{lower}} = 0.95$, $f_{3,\text{lower}}=0.94$, $f_{1,\text{upper}}=0.98$, $f_{3,\text{upper}}=0.97$ resulting in a mean $f \sim 0.96$. This shows that the northern California Coast Range landslides can be approximately represented as blocks sliding on a slope. Therefore, for our thickness inversions we set $f = 1$. Changing f does not impact the spatial pattern of thickness from the inversions, but does impact the magnitude as the inverted thickness scales as $h \sim 1/f$ (Booth, Lamb, et al., 2013). Setting $f = 0.96$ will cause a 4% increase in thickness for each landslide (Table S3).

Text S2.

Generalized Cross Validation (GCV)

We use GCV to select the appropriate value of the damping parameter for each landslide, which is defined as the value of alpha that minimizes the function

$$g(\alpha) = \frac{m\|Xh_\alpha - b\|_2^2}{Tr(I - XX^{\#})^2}, \qquad \text{(S2)}$$

where m is the length of vector h, h_α is the inferred thickness for a specific value of α, Tr indicates the trace of a matrix, I is the identity matrix, and $X^{\#}$ is the pseudo-inverse of X, defined as

$$X^{\#} = (X^T X + \alpha^2 B^T B)^{-1} X^T, \qquad \text{(S3)}$$

where the superscript T indicates the transpose, and the superscript –1 indicates the inverse of a matrix. For our landslide data, $g(\alpha)$ always had an unambiguous minimum, which allowed for objective determination of the appropriate α for each landslide. In contrast, other common

methods that have been applied to landslide thickness inversions, such as the *L*-curve criterion (Delbridge et al., 2016; Booth et al., 2020), required subjective interpretation for our northern California Coast Ranges landslide data.

Uncertainty estimation

Uncertainty on the inferred landslide thickness is a result of two general sources: systematic errors (bias) introduced by regularization, nonnegative constraints, and the assumed model physics and random errors in the observations (surface velocities and topographic data). Quantifying the magnitudes of systematic errors would require independent information on true landslide depths, which is not available for the northern California Coast Ranges landslides analyzed in this study. For the random errors, we estimate uncertainties on the surface velocity data, but do not have a reliable estimate for uncertainty on the topographic data, which is also included in the vector of observations, *b*. Furthermore, horizontal velocity components are included in both the matrix *X* and vector *b*, while standard methods of uncertainty estimation for inverse problems assume errors only in *b*. A complete assessment of thickness uncertainty for the population of landslides analyzed is therefore not feasible, but we nonetheless can make a reasonable estimate of the minimum uncertainty on landslide thickness given an estimate of the uncertainties on the data in vector *b* following standard inverse theory.

First, to estimate the uncertainty on *b* (which we quantify here as its variance, σ_b^2), we calculate the model residuals, *r*, for the inferred thickness model as

$$r = Xh_\alpha - b \quad . \qquad \text{(S4)}$$

Since the residuals by definition quantify the misfit between the predicted and observed data, the variance of the residuals (σ_r^2) approximates the variance of *b* (σ_b^2) (Aster et al., 2013). The variance of *h* (σ_h^2) can then be estimated using

$$\sigma_h^2 = \sigma_b^2 \, diag(X^{\#} X^{\#^T}), \qquad \text{(S5)}$$

where *diag* indicates the vector corresponding to the main diagonal of $X^{\#}$ (Kasper et al., 2002). This assumes that the covariance of *b* is $\sigma_b^2 I$, implying that the uncertainty on *b* is spatially constant, independent, and normally-distributed. In general, uncertainties on *b* may vary in space and be correlated with neighboring pixels, but as long as the covariance matrix is diagonally dominant, this still provides a reasonable estimate.

We calculated σ_h for a sample of seven landslides representing the variety of style, size, and shape found in the study population. Uncertainties ranged from ±1 to ±11 m, and the mean value of all sampled landslides was ±2.4 m. Uncertainty was generally lowest throughout the center of the landslide, and increased near its edges (Figure S3). That was likely an effect of the mask applied at the boundary of each landslide to force inferred thickness to be ~0 outside of the active landslide. For the seven sampled landslides, their average thickness uncertainty increased with landslide size (Figure S3), ranging from ±1.5 to ±3.8 m from the smallest to largest landslide sampled.

Supplementary Figures

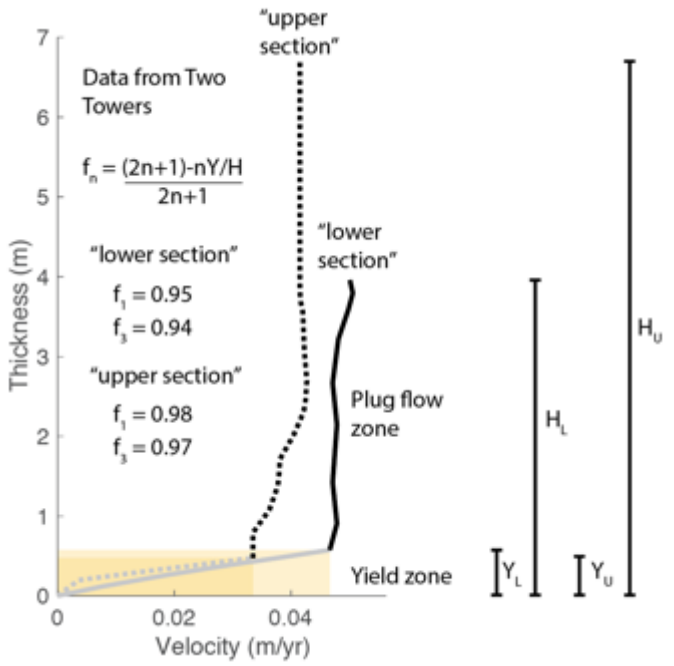

Figure S1. Borehole inclinometer data for the Two Towers landslide, northern California Coast Ranges (see location in Figure 1). Thickness corresponds to the height above the sliding surface. The two lines show data from the "upper" and "lower" field sites. The landslide has a narrow yield zone (shown by yellow box) with plug flow for the majority of the landslide thickness. These data show that the northern California Coast Ranges can be approximated as blocks sliding on a slope. Data are from Schulz et al., 2018.

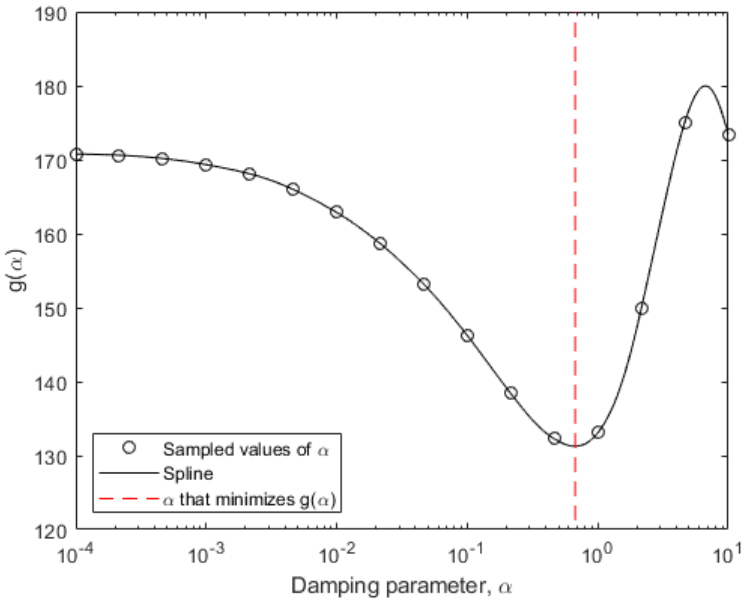

Figure S2. Example Generalized Cross Validation (GCV) function for landslide thickness inversion. This shows the GCV for landslide A2 (see landslide in Figure S3). The appropriate value of α (dashed red vertical line) is selected to minimize equation S2.

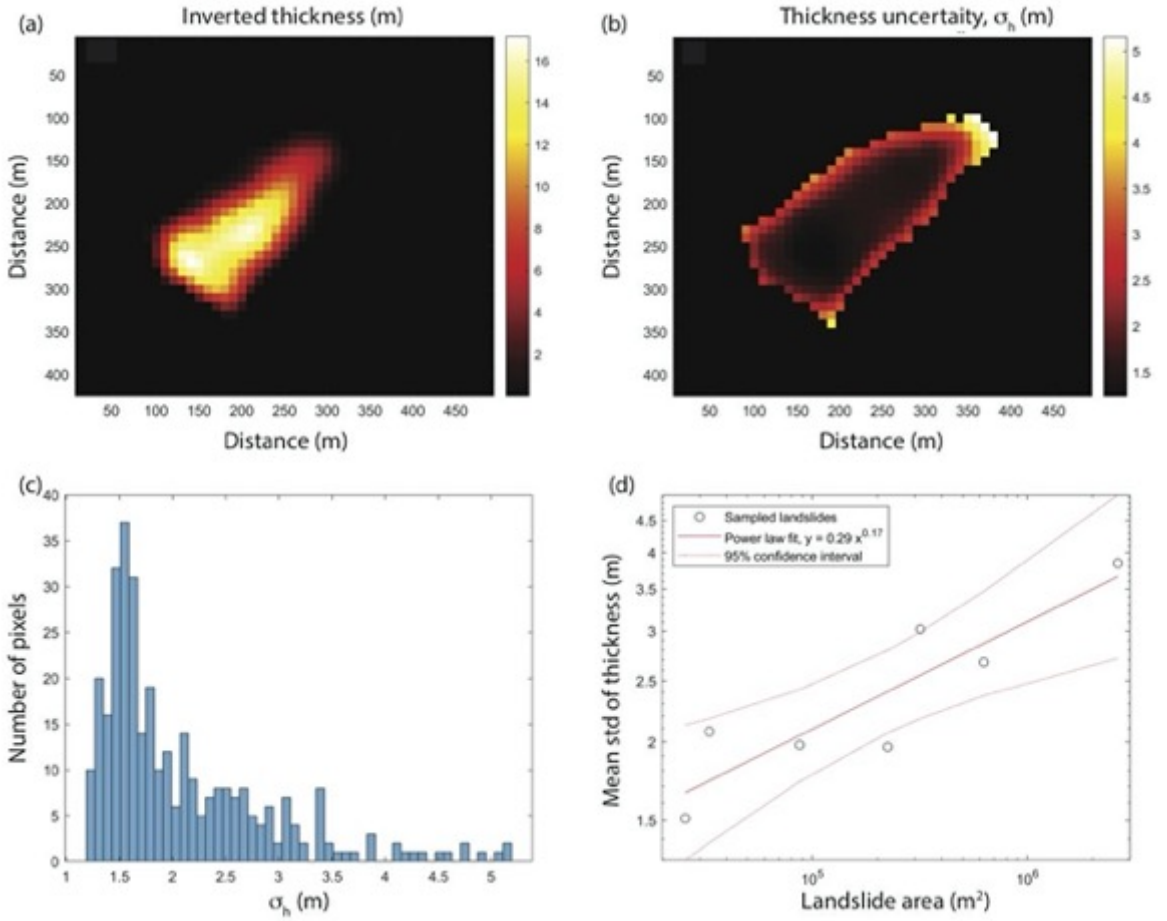

Figure S3. Landslide thickness inversion uncertainty. Maps of (a) Inferred thickness and (b) uncertainty on thickness for landslide "A2". (c) Histogram of thickness uncertainties. (d) Mean standard deviation of inferred landslide thickness (σ_h) vs. landslide area for the representative sample of landslides. Solid red line is a power law fit, and dashed red line is the 95% confidence interval.

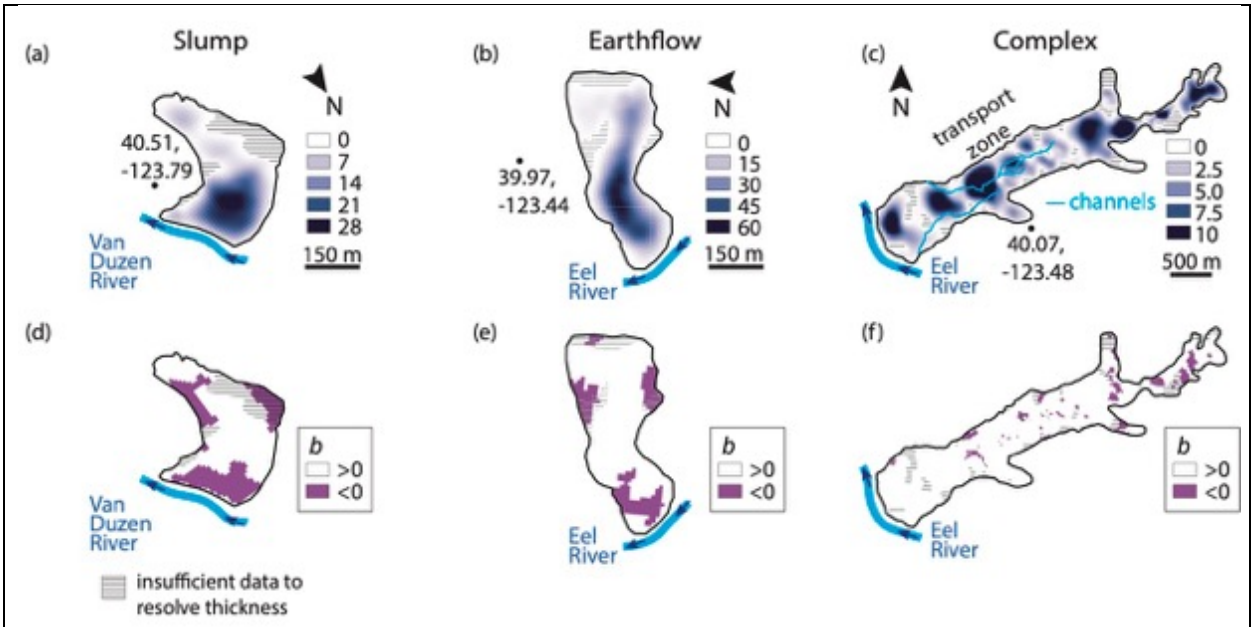

Figure S4. Landslide thickness inversions for example slump, earthflow, and landslide complex. (a–c) Landslide thickness maps. Black dots show latitude and longitude coordinates. Thick blue lines show rivers and thin blue lines show deep channels incised into the landslide body. (d–f) Vector *b* maps (equation 4). Negative *b* values show areas that have a negative flux divergence where the landslide is expected to thin. Hachures show zones with insufficient data to resolve thickness.

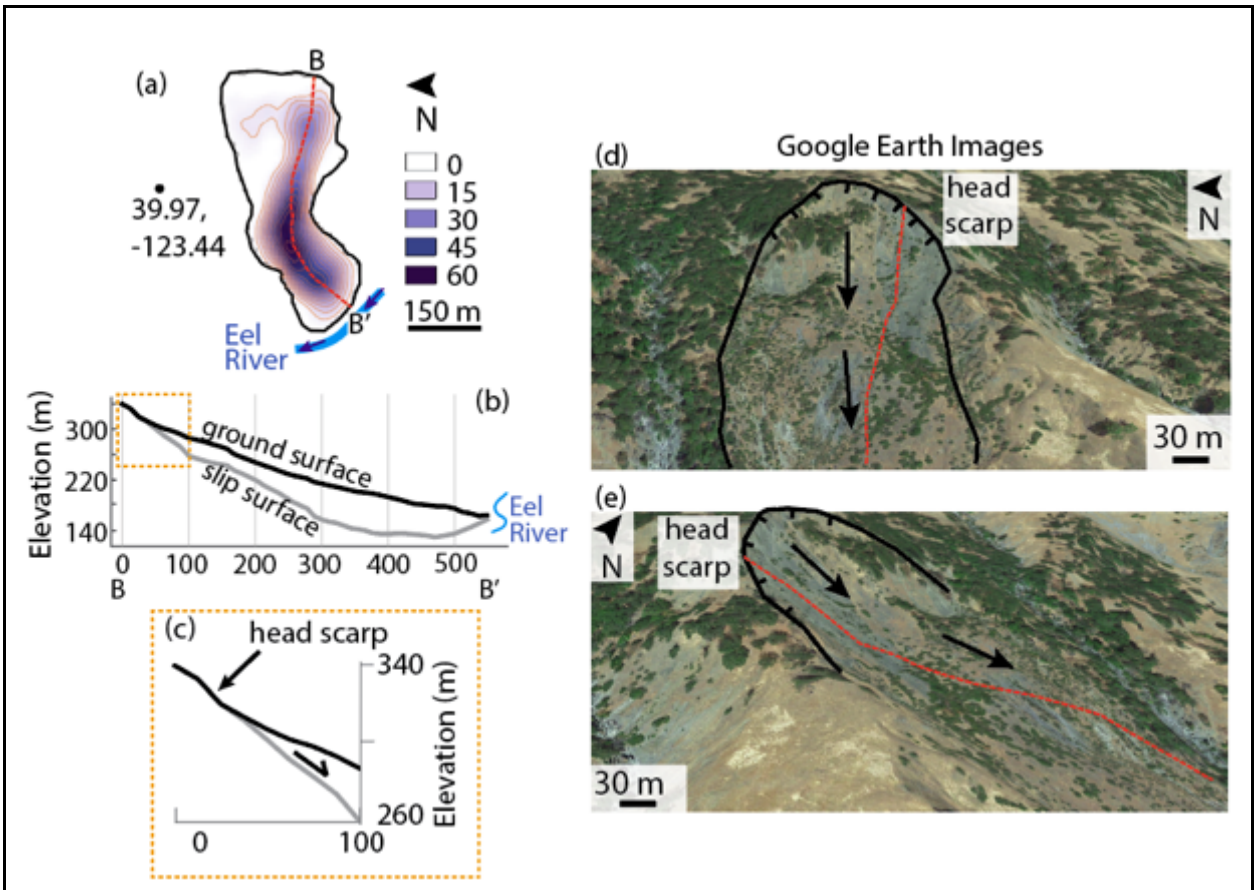

Figure S5. Landslide thickness inversions and Google Earth imagery for the example earthflow. This is the same landslide shown in Figures 2 and 3. (a) Landslide thickness maps. Thin yellow lines with labels show 5-meter thickness contours. Red dashed line shows profiles plotted in (b, c). Black dot shows latitude and longitude coordinates. Thick blue line shows the location of the Eel River. (b) Ground surface and slip surface elevation profiles. (c) Zoom-in of landslide headscarp. Black arrows show sliding direction. (d,e) Oblique view of Google Earth Imagery showing the well-defined headscarp. The headscarp can be used to trace the sliding surface beneath the ground surface (c). The extension of the headscarp slip surface under the landslide provides confirmation that the inversion is approximating the slip surface elevation correctly.

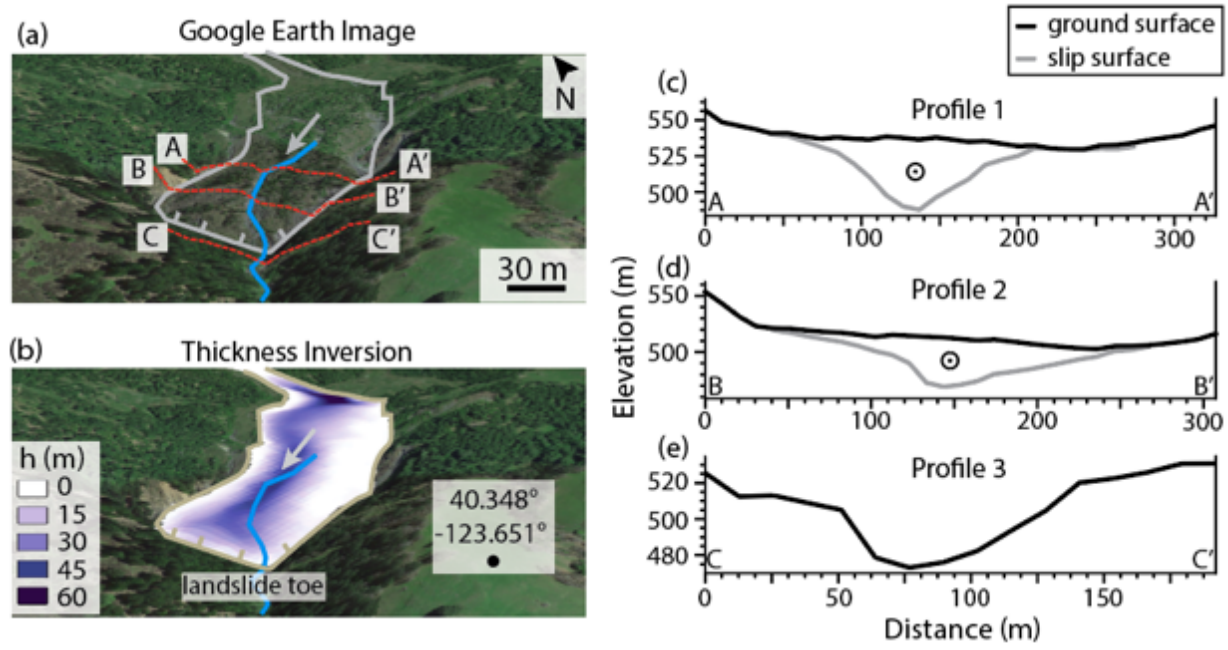

Figure S6. Thickness and elevation profiles for a slow-moving landslide that has filled in a pre-existing valley. (a) Oblique view of a Google Earth image showing the slow-moving landslide that has filled in the valley. Blue line shows the channel profile on and off the landslide. Gray line shows the landslide boundaries with an arrow showing the general direction of motion. Red dashed lines show location of profiles shown in (c-e). (b) Thickness map draped over the Google Earth image. Black circle shows latitude and longitude at that location. (c-d) Ground surface (black lines) and inverted slip surface (gray lines) profiles across the valley filling landslide. Black circle with dot indicates motion out of the page. (e) Ground surface profile showing the current incised channel that is downslope of the landslide toe. The extension of the valley shown by the inverted slip surface provides confirmation that the inversion is approximating the slip surface elevation correctly

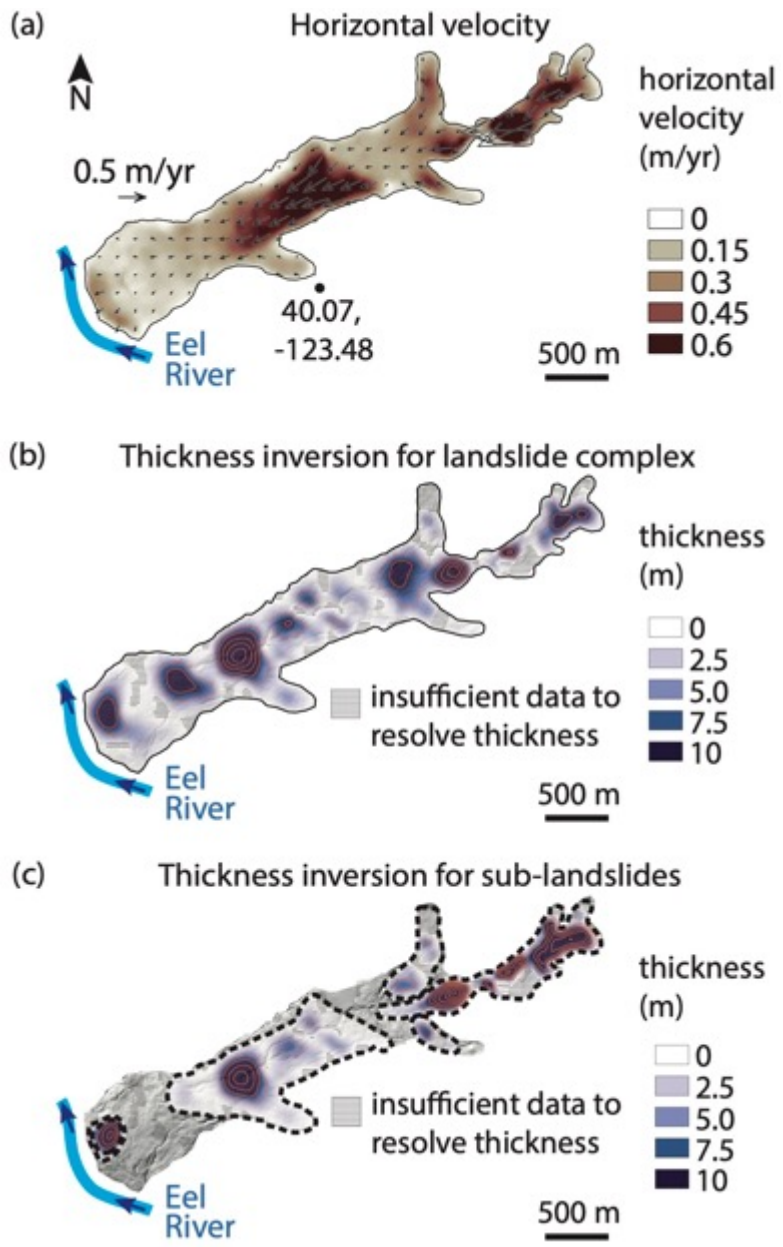

Figure S7. Multiple thickness inversions for the Boulder Creek landslide complex. (a) Horizontal velocity map. Black arrows show horizontal velocity vectors. (b) Thickness inversion for the entire landslide complex. Note we had to downsample the inversion for the full landslide complex to a 20 m pixel grid due to computational limitations. (c) Thickness inversion for multiple sub-landslides within the Boulder Creek landslide complex. Hachures show zones with insufficient data to resolve thickness. Here we split the landslide complex into five smaller landslides. The thickness pattern is similar for both inversions. Contours show 5-m thickness. Some of the differences in the magnitude of the thickness are explained by the different spatial resolutions used in the inversions (i.e., 10 m pixel or 20 m pixel).

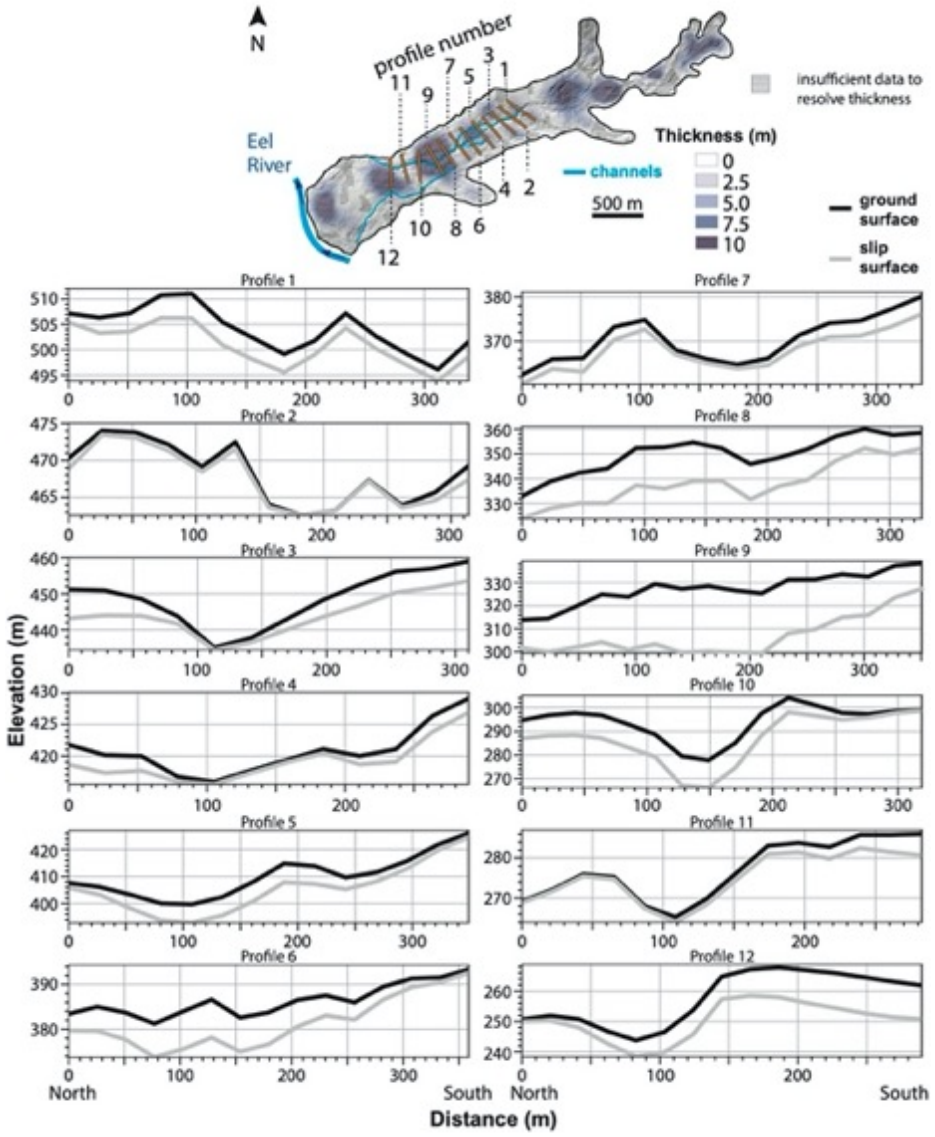

Figure S8. Thickness inversion for the Boulder Creek landslide complex. Map view shows the thickness inversion for the full landslide. Hachures show zones with insufficient data to resolve thickness. Blue lines correspond to channels. Orange lines correspond to location of profiles 1-12. Profiles show ground surface (black lines) and slip surface (gray lines) elevation. The thickness inversion for this landslide produced patches deep and shallow zones in the center of this landslide. Many of these changes in landslide thickness result from a deep (15-20) channel network that has incised into the landslide body. The patchy thickness inversion results indicate that the slip surface depth is close to the channel depth in many places.

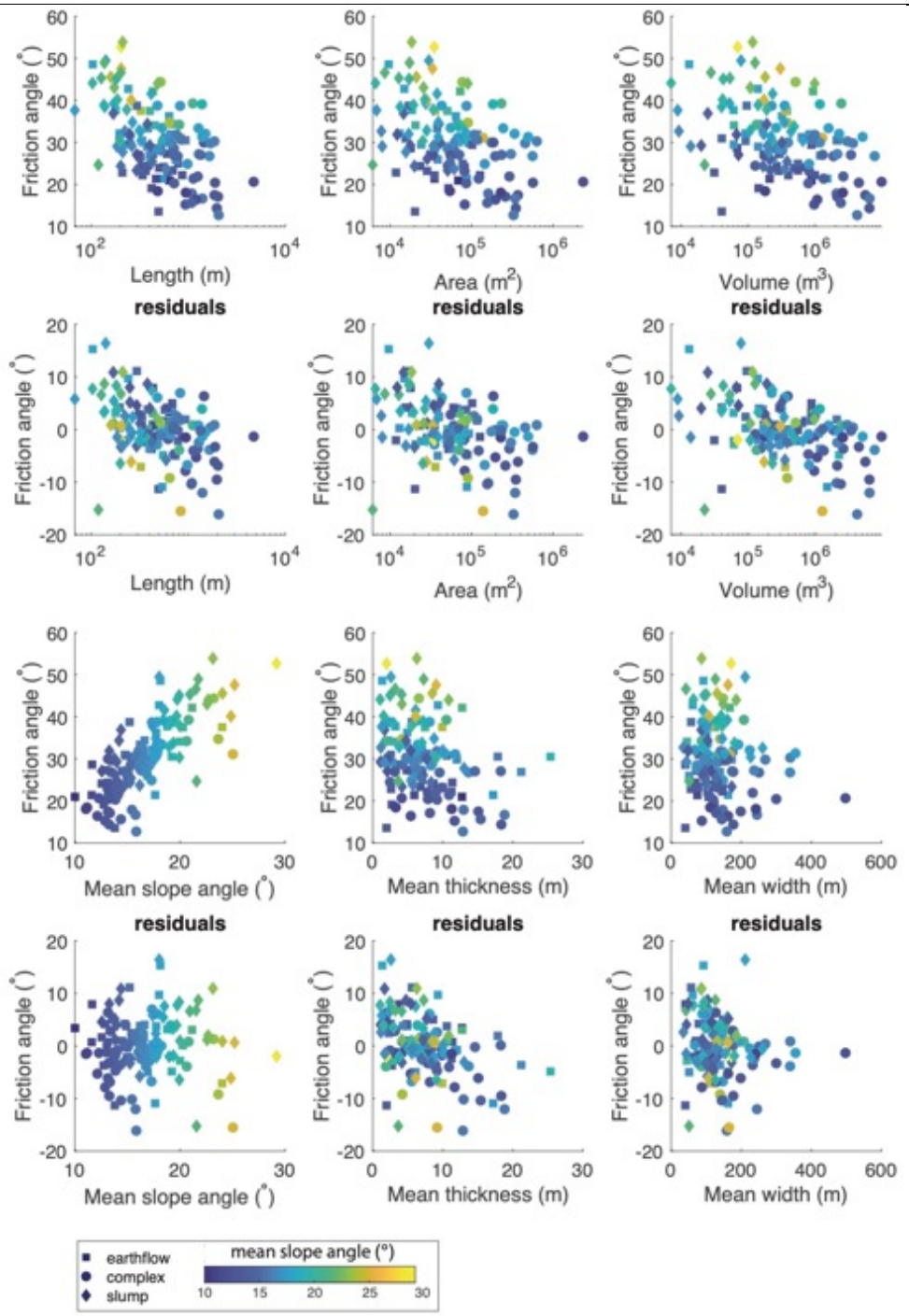

Figure S9. Inferred friction angle and friction angle residuals for saturated end-member conditions. Friction angle and friction angle residuals are compared to landslide length, area, volume, mean slope angle, mean thickness, and mean width. The residuals are calculated by subtracting the linear fit to slope angle and friction angle (Figure 6a). After removing the dependence on slope angle, we find important and interesting relations between landslide size and inferred strength.

Table S1. List of pixel offset tracking pairs. Columns correspond to the pair number, acquisition dates of pixel offset tracking pairs, the timespan between images. The same pairs were processed for all 4 UAVSAR flight tracks. The file contains has two spreadsheets. The spreadsheet named "pairs used for analyses" shows only the pixel offset pairs used in our study. The spreadsheet named "all processed pairs" includes all of pixel offset pairs that were processed.

Table S2. Parameter values used in computations

Parameter name and units	**value**	**Source**
gravity, m/s^2	9.8	
dry density of landslide material, kg/m^3	1837	Schulz et al. (2018)
saturated density of landslide material, kg/m^3	2143	Schulz et al. (2018)
density of water, kg/m^3	1000	

Table S3. Landslide inventory data table. Table includes landslide statistics for geometry, 3D velocity, stress and strength, inversion parameters, and the centroid location of each landslide. The table has two spreadsheets. The spreadsheet named "low thickness pixels excluded" shows the landslide statistics after the low thickness zones (< 0.1 m) were excluded. The spreadsheet named "all pixels" shows the landslide statistics for the fully mapped landslide.

Table S4. Volume-area scaling $V = c_V A^{\gamma}$ and Thickness-area scaling $h = c_h A^{\zeta}$ (with 95% confidence bounds). Fit values are included for landslides with (grey text) and without (blue text) low thickness zones (< 0.1 m).

category	c_V, best fit intercept excluding low thickness zones	γ, best fit power function exponent excluding low thickness zones	R^2	*p-value*	c_h, best fit intercept excluding low thickness zones	ζ, best fit power function exponent excluding low thickness zones	R^2	*p-value*
inventory	0.2074 (0.0746, 0.5761)	1.306 (1.213, 1.399)	0.8541	~0	0.2074 (0.0746, 0.5761)	0.3058 (0.2129, 0.3987)	0.2430	~0
slumps	0.0301 (0.0020, 0.4569)	1.493 (1.224, 1.762)	0.7491	~0	0.0301 (0.0020, 0.4569)	0.4926 (0.2236, 0.7615)	0.2454	0.0006
earthflows	0.0207 (0.0013, 0.3389)	1.535 (1.273, 1.796)	0.7787	~0	0.0207 (0.0013, 0.3389)	0.5348 (0.2734, 0.7963)	0.2994	0.0002
complexes	0.9542 (0.1029, 1.2674)	1.172 (0.9858, 1.357)	0.7779	~0	0.9542 (0.1029, 1.2674)	0.1716 (-0.0142, 0.3573)	0.0699	0.0694
category	c_V, best fit intercept including low thickness zones	γ, best fit power function exponent including low thickness zones	R^2	*p-value*	c_h, best fit intercept including low thickness zones	ζ, best fit power function exponent including low thickness zones	R^2	*p-value*
inventory	0.1274 (0.0338, 0.4781)	1.324 (1.206, 1.442)	0.7885	~0	0.1274 (0.03388, 0.4781)	0.3243 (0.2063, 0.4424)	0.1828	~0
slumps	0.01901 (3.69e-4, 0.9813)	1.502 (1.121, 1.883)	0.6014	~0	0.01901 (3.690e-4, 0.9813)	0.5018 (0.1211, 0.8826)	0.1442	0.0110
earthflows	0.03491 (5.636e-4, 2.163)	1.453 (1.075, 1.831)	0.6016	~0	0.03491 (5.636e-4, 2.163)	0.453 (0.07515, 0.8308)	0.1280	0.0200
complexes	0.6937 (0.05546, 8.672)	1.182 (0.9739, 1.389)	0.7402	~0	0.6937 (0.05546, 8.672)	0.1817 (-0.02609, 0.3895)	0.0631	0.0850